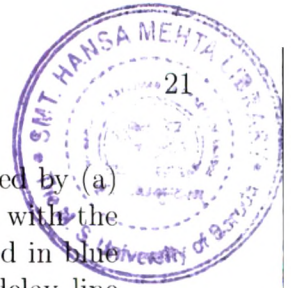


List of Figures

1.1	Energy of the first excited 2_1^+ state versus the neutron number N [2].	27
1.2	$B(E2;0^+ \rightarrow 2^+)$ values [2] across the nuclear chart for even-even nuclei in units of a single particle value defined as $B(E2;0^+ \rightarrow 2^+)_{s.p.u.} = 3 \cdot 10^{-5} A^{\frac{4}{3}} e^2 b^2$ [3].	28
1.3	Partial level schemes [NNDC] and isomer systematics in the even- A Sn nuclei for mass numbers between $A = 102$ and $A = 130$. Levels of the same spin and positive parity are connected by broken lines.	29
2.1	Schematic illustration of geometrical interpretation of short-range residual interaction for two particle configuration j_1 and j_2	34
2.2	A geometrical analysis of the $ (g_{7/2})^2, J\rangle$ multiplet in ^{112}Sn . The angular dependence of the δ -function residual interaction strength is shown on the left with the semiclassical angle for the two identical particles in the equivalent orbits ($T=1$).	35
2.3	Partial level schemes [NNDC] in the even- A Sn nuclei for mass numbers between $A=102$ and $A=130$	37
2.4	$B(E2 \uparrow)$ values in the even- A Sn nuclei for mass numbers between $A=106$ and $A=130$. The data are from NNDC and [6, 14, 15, 16].	38
2.5	Measured E2 transition matrix elements for the $(\nu h_{11/2})^n 10^+ \rightarrow 8^+$ transitions in even- A Sn isotopes [17, 18].	38
3.1	Sommerfeld parameter η (eq. 3.1) as a function of the target charge number Z_2 for various projectiles at the safe bombarding energy (eq. 3.16).	40
3.2	Classical picture of the ^{58}Ni projectile orbit ($\theta_{cm}=120^\circ$) in the Coulomb field of the ^{112}Sn nucleus at 175MeV. The hyperbolic orbit of the projectile is shown in the relative frame of reference where the target is at rest. The nuclear charge radii are displayed (for details see text) as well as the nuclear interaction radius (dashed dotted lines).	41
3.3	Schematic picture of an extended charge distribution (see text)	43
3.4	Inelastic cross section for the single-step 2^+ excitation in ^{112}Sn	46

3.5	Particle- γ angular correlation for ^{58}Ni projectiles scattered at angles of $\theta_{cm}=45^\circ$ and $-9^\circ \leq \phi_{cm} \leq 9^\circ$ (full curve) and $81^\circ \leq \phi_{cm} \leq 99^\circ$ (dashed curve). The γ -rays of the $2^+ \rightarrow 0^+$ transition in ^{112}Sn are measured with Ge-detectors in plane ($\phi_\gamma=0^\circ$ or $\phi_\gamma=180^\circ$). The beam and target is indicated as well as the scattering at $\theta_{cm}=45^\circ$	48
3.6	γ -ray angular correlation for $2^+ \rightarrow 0^+$ transition in ^{112}Sn after the scattering of ^{58}Ni projectiles at an angle of $\theta_{cm}=45^\circ$. The calculation was performed without taking into account the deorientation effect ($G_k=1$) and the integration over a finite size of the Ge detector ($Q_k = 1$). The dashed line shows an isotropic γ -ray angular correlation.	49
4.1	Particle- γ coincidence set-up at GSI (left) and at IUAC (right).	51
4.2	Schematic view of the experiment performed at IUAC. A position sensitive annular gas-filled parallel plate avalanche counter (PPAC) was placed in forward direction covering the angular range of $15^\circ \leq \vartheta_{lab} \leq 45^\circ$. Four Clover detectors were mounted at $\vartheta_\gamma \sim 135^\circ$ with respect to the beam direction. . .	52
4.3	Kinematics of Coulomb excitation experiments with ^{114}Sn beam on ^{58}Ni target (left) and with ^{58}Ni beam on ^{112}Sn target (right). Energy dependence of both reaction partners is plotted as a function of the scattering angle in the centre of mass system (θ_{cm}) and laboratory frame (ϑ_3, ϑ_4). Solid lines correspond to projectile-like fragment and the dashed lines correspond to target-like fragments.	54
4.4	Scattered projectiles and target nuclei coincidences were detected in the PPAC for the ^{116}Sn beam incident on the ^{58}Ni target. The scattering angle is plotted versus the flight time differences of both reaction partners. The corresponding kinematical cuts applied for coincident γ -rays are indicated. See text for details.	54
4.5	Kinetic energies of the scattered ^{58}Ni projectiles and ^{112}Sn recoils detected in the angular range of 15° to 45° covered by the PPAC. The dashed lines are based on two body kinematics for a beam energy of 175 MeV, while full lines are corrected for energy loss [32] in a $10 \mu\text{m}$ MYLAR foil, which was used as entrance window of the PPAC.	55
4.6	Block diagram showing the electronics used for the Coulomb excitation experiments at IUAC. (CFD: constant fraction discriminator, SH: shaper, GG: gate generator, A(T)DC: analog-(time)-to-digital-converter).	56
4.7	Ungated γ -ray spectrum from Clover-2 detector (IUAC experiment) in coincidence with scattered projectiles measured in the particle detector.	57
4.8	Doppler corrected γ -ray spectra associated with a coincidence of two particles in the PPAC. The Doppler correction (case 4) was applied using kinematical information of the target nuclei (^{58}Ni cuts in fig. 4.4), but assuming a projectile excitation of ^{114}Sn (left) and ^{116}Sn (right), respectively. The elevation between 1400keV and 1600keV corresponds to decays from the 2_1^+ state of the ^{58}Ni ejectiles. In order to obtain narrow peaks for the target excitation of ^{58}Ni , the same data were used but the Doppler correction (case 3) was applied to obtain the lower spectra.	60



5.1	Ungated γ -ray spectrum for Clover-2 (black) and γ -ray spectra gated by (a) left delay-line and (b) right delay-line. The spectra in coincidence with the small angle end of the delay line (inner contact readout) are plotted in blue while the spectra in coincidence with the large angle end of the delay line (outer contact readout) are plotted in red. For all spectra the add-back procedure was applied.	63
5.2	Gamma-particle time-of-flight (TOF) spectrum (black) and γ -energy gated spectra for Ni(blue, $E_\gamma=1264\text{keV}$) or Sn(red, $E_\gamma=1200\text{keV}$) particles detected in PPAC.	64
5.3	γ -spectra associated with the random events (bottom red curve) and background-subtracted prompt spectrum (top black curve).	65
5.4	Total number of counts recorded for each φ -segment during the γ -p coincidence measurement (black curve). The blue and red histograms show the corresponding counts in coincidence with signals from inner and outer contacts of the delay-lines.	65
5.5	Top panel shows the SDL readout for different φ -segments: #1(black), #8(blue), #16(red), #19(green) and #4(black), #7(blue), #11(red) and #17(green). In the bottom panel the corresponding spectra are shown in coincidence with the outer contact.	66
5.6	DDL spectra for segments 1-10 (black) and segments 11-20 (red). The count rates in both halves are different as there were some of the φ -segments not working during the experiment.	67
5.7	SDL spectrum gated by different regions of the DDL spectrum (see fig. 5.6) (i)black - ungated, (ii)green full DDL range, (iii)blue L-region, (iv)red M-region and (v)pink H-region (see text for details)	68
5.8	Doppler corrected γ -ray spectra for individual crystals of Clover-2 assuming a common correction ($\vartheta_\gamma, \varphi_\gamma$) for the Clover.	69
5.9	Doppler oscillations for Crystal-1 of Clover-2. The circles are experimental centroids for Ni and Sn peaks for gate-M of the DDL spectrum (fig. 5.6). The solid curves correspond to the theoretical predictions for $E_{lab}=167\text{MeV}$, $\vartheta_p=32.9^\circ$, $\vartheta_\gamma=142.7^\circ$ and $\varphi_\gamma=143.2^\circ$ (see text). For Sn γ -rays, theoretical curves for two different beam energies $E_{lab}=167\text{MeV}$ and 138MeV are shown. (see also Appendix A.3)	70
5.10	Calculated Doppler-shifted peak positions for projectile and target excitation as a function of detector angle ϑ_p . The energy loss in the target was neglected in the above calculations.	70
5.11	Doppler corrected γ -ray spectra for the systems $^{112}\text{Sn}+^{58}\text{Ni}$ (blue)	72
5.12	Doppler corrected add-back spectra for Clover-2. The black and red curves correspond to spectra under 'prompt' and 'random' conditions in Clover-PPAC TOF spectrum. The top and bottom spectra correspond to Doppler corrections assuming projectile (Ni) excitation and target (Sn) excitation.	73

5.13	Doppler corrected add-back spectra for Clover-2. The black and red spectra correspond to correlations for $-90^\circ < \varphi_{\gamma p} < 90^\circ$ and $90^\circ < \varphi_{\gamma p} < 270^\circ$. The top and bottom sets correspond to Doppler corrections assuming projectile and target excitations.	75
6.1	Two-neutron separation energy S_{2n} for the tin isotopes as a function of the neutron number.	79
6.2	Effective charge for a neutron induced by the attractive strong interaction between single nucleon and the core.	82
6.3	Graphical representation of a particle in an orbital j , polarizing the core towards oblate deformation with a negative quadrupole moment (left), and a hole in an orbital giving rise to a prolate core polarization (right).	83
6.4	The increase in the absolute value of the quadrupole moments of isomers in the Pb region has been understood as due to a coupling of the valence particles with the quadrupole excitations of the underlying core.	83
6.5	Experimental data on $B(E2; 0_{g.s}^+ \rightarrow 2_1^+)$ values in the Sn isotope chain from the current results for $^{112,114}\text{Sn}$ and from [2, 6, 14, 15, 16]. The dotted and the full lines show the predictions of the large-scale shell model calculations [6] performed with a ^{100}Sn core and a ^{90}Zr core, respectively.	85
6.6	The attractive scalar field $S(r)$ and the repulsive vector field $V(r)$ form the weak nuclear mean field $(S+V)$ and the strong spin-orbit term $(S-V)$	86
6.7	Experimental data on $B(E2; 0_{g.s}^+ \rightarrow 2_1^+)$ values in the Sn isotope chain from the current results for $^{112,114}\text{Sn}$ and from [2, 6, 14, 15, 16]. The full line shows the predictions of the RQRPA calculations [54]	89
7.1	Schematic drawing of the W1(DS)-1000 double-sided silicon strip detector (DSSSD) from Micron Semiconductor Ltd [59].	92
7.2	Schematic drawing of the position correlation between the projectile implant and the subsequent β -decay measured with the double-sided silicon strip detector (DSSSD).	92
7.3	Simulated energy spectrum of β -particles emitted from fragments implanted uniformly (solid line) and exactly in the centre (dashed line) of a DSSSD (left). The simulation assumes a Q_β -value of 5MeV and a Fermi-Curie distribution for β -particles. The right figure shows the calculated β -detection efficiency as a function of the DSSSD threshold for the two considered implantation scenarios.	93
7.4	Output signal of the MPR-32 preamplifier for a ^{207}Bi β -source (pulse-height 200mV, decay time $30\mu\text{s}$)	94
7.5	The characteristics of the logarithmic MPR-32 preamplifier was measured with a 10 MeV linear range setting and STM-16 spectroscopy amplifiers.	94
7.6	Energy spectra of a ^{207}Bi β -source measured for different discriminator thresholds labelled T=8 to T=32 of the Mesytec STM-16 module.	95
7.7	Energy spectrum of a ^{241}Am α -source measured with DSSSD-2512-17 front strip X4 (left) and back strip Y4 (right).	96

7.8	Strip multiplicity for front (left) and back (right) side measured for DSSSD-2512-17 at a bias voltage of 40V (detector not fully depleted) for α -particles of a ^{241}Am source.	96
7.9	3-D histogram of x-position versus y-position measured for DSSSD-2243-5 with α -particles of a ^{241}Am source. The source is centred (left) and off-centre (right) relative to the DSSSD.	97
7.10	The conversion electron spectrum of ^{207}Bi obtained by strip X4 of DSSSD-2512-17. Four peaks at 482keV, 555keV, 976keV and 1049keV are by mono-energetic electrons (left). The energy resolution for the front junction and the rear ohmic side versus the strip number is plotted on the right side.	97
7.11	The conversion electron spectrum of ^{207}Bi obtained by strip X3 of DSSSD-2243-5 measured with the linear MPR-32 (top) and the logarithmic MPR-32 (bottom). The energy resolution and the signal-to-noise ratio are $\Delta E=15.3\text{keV}$ and 3.5:1 for the linear MPR-32 and $\Delta E=19.7\text{keV}$ and 2.6:1 for the logarithmic MPR-32, respectively.	98
7.12	Output signal of the CPA-16 preamplifier for a ^{207}Bi β -source.	99
7.13	The conversion electron spectrum of ^{207}Bi obtained by a strip of DSSSD-2243-5. Two peaks at 482keV and 976keV are by mono-energetic electrons. The high gain output signal of the CPA-16 preamplifier was sent directly to the ADC.	100
7.14	The ratio of the γ -transmission of aluminium and the printed circuit board material Pertinax is plotted as a function of the Al-layer. The γ -transmission of both materials is equal for a thickness of 2mm aluminium	101
7.15	The Cluster array of the stopped beam RISING experiments with the active stopper vessel made out of Pertinax (left) and the top cover of the active stopper chamber with the cable connectors (right) for six DSSSD arranged in two rows.	101
7.16	Schematic layout of the RISING set-up at the final focal plane area (S4) of the FRagment Separator (FRS) at GSI. The beam diagnostic elements consist of two multiwire detectors (MW41 and MW42), two ionisation chambers (MUSIC) and two scintillation detectors (Sc21 and Sc41). The degrader allows an accurate implantation of the heavy ions in the active stopper, which is surrounded by Ge-Cluster detectors for γ -ray measurement.	102
7.17	Measured energy spectra (10MeV range of the linear MPR-32 preamplifier) obtained by x-strips (front junction) of DSSSD-2243-5 for the implantation of ^{136}Xe ions.	103
7.18	Multiplicity distributions measured by x-strips of DSSSD-2243-5 for different energy thresholds. For a very low threshold (channel number 200) almost all x-strips are firing, while for the overflow ($>10\text{MeV}$) data the hit probability is very low, as expected for the implantation of ^{136}Xe ions.	104

7.19	Position correlation between the multiwire detector MW and the DSSSD-2243-5. In case of the DSSSD the position of the implanted ^{136}Xe ion was determined from the overflow data, when a linear MPR-32 preamplifier was used.	104
7.20	Measured energy spectra (10MeV range for the linear part of the logarithmic MPR-32 preamplifier) obtained by x-strips (front junction) of DSSSD-2243-5 for the implantation of ^{136}Xe ions. The double hump structure is related to the stopping of the heavy ions.	105
7.21	Multiplicity distribution for the higher peak of the double hump structure (left). The black distribution shows the result for all x-strips of DSSSD-2243-5, while for the red one strip=1 was removed, which seemed to be very noisy. The right diagram shows the hit pattern relative to the strip with the highest peak for multiplicity 2 events. In 90% of all cases the second highest peak is in a neighbouring strip.	106
7.22	Position correlation between the multiwire detector MW and the DSSSD-2243-5. In case of the DSSSD the position of the implanted ^{136}Xe ion was determined from the mean of highest peak, when a logarithmic MPR-32 preamplifier was used. The left correlation includes all strips, while for the right one a single noisy strip was removed.	106
7.23	Delayed charged particle spectrum associated to ^{205}Au . In addition to the continuous energy of the β -decay, two peaks are observed. These are interpreted as K and L internal conversion electron peaks corresponding to a 907(5) keV transition.	108
8.1	Schematic picture of detector assembly for AIDA	111